39th AIAA Fluid Dynamics Conference
22 - 25 June 2009, San Antonio, Texas

AIAA 2009-3559

Instability and Transition Measurements in the Mach-6 Quiet Tunnel

Brad M. Wheaton*, Thomas J. Juliano*, Dennis C. Berridge*, Amanda Chou*,
Peter L. Gilbert*, Katya M. Casper*, Laura E. Steen*, and Steven P. Schneider†
School of Aeronautics and Astronautics, Purdue University, West Lafayette, IN 47907-1282

Heath B. Johnson‡
Department of Aerospace Engineering and Mechanics, University of Minnesota, Minneapolis, MN 55455

The Boeing/AFOSR Mach-6 Quiet Tunnel achieved quiet flow to a stagnation pressure of 163 psia in Dec. 2008, the highest value observed so far. It remains quiet at pressures above 160 psia. Under noisy conditions, nozzle-wall boundary-layer separation and the associated tunnel shutdown appear to propagate slowly upstream, whereas under quiet conditions, the propagation is very rapid. A new diffuser insert has been designed, fabricated, and installed in the tunnel in order to start larger blunt models and increase run time. A flared cone with a circular-arc geometry was designed to generate large second-mode N factors under quiet flow conditions. When the computed N factor was 13, large instability waves were measured under quiet flow conditions using fast pressure sensors, but the flow remained laminar. Transition was observed only under noisy conditions. A laminar instability was detected in the wake of an isolated roughness element in the boundary layer on the nozzle wall; this appears to be the first such measurement at hypersonic speeds.

Nomenclature

α_i	growth rate (1/m)
ρ	density ($\frac{kg}{m^3}$)
ρu	mass flux ($\frac{kg}{m^2 s}$)
θ_i	cone initial half angle (deg)
A	disturbance amplitude
A_0	initial disturbance amplitude
f	frequency (kHz)
k	roughness height (mm)
L	cone length (m)
M	Mach number
N	integrated amplification factor
P	pressure (psia)
R	cone radius of curvature (m)
Re	Reynolds number
s	cone arc-length coordinate (m)
t	time (s)
T	temperature (K)
V	voltage (V)
x	cone axial coordinate (m or cm)
y	cone radial coordinate (m)
y^+_{wall}	dimensionless wall parameter
z	tunnel axial coordinate (0 at throat) (m)

Subscript

∞	freestream condition
θ	momentum thickness
0	stagnation
i	initial conditions
e	edge conditions
$Wall$	wall condition

Superscript

$'$	fluctuations

Abbreviations

BAM6QT	Boeing/AFOSR Mach-6 Quiet Tunnel
LST	Linear Stability Theory
PSE	Parabolized Stability Equations
RMS	Root Mean Square

*Research Assistant, Student Member AIAA
†Professor, Associate Fellow AIAA
‡Senior Research Associate, AIAA Senior Member

I. Introduction

The understanding of laminar-turbulent transition in hypersonic boundary layers is important for prediction and control of heat transfer, skin friction, and other boundary layer properties. Vehicles that spend extended periods at hypersonic speeds may be critically affected by the uncertainties in transition prediction, depending on their Reynolds numbers. However, the mechanisms leading to transition are still poorly understood, even in low-noise environments.

Algebraic correlations based on parameters such as Re_θ/M_e (Reynolds number based on boundary-layer momentum thickness divided by edge Mach number) are commonly used to estimate transition location. Linear Stability Theory (LST) and Parabolized Stability Equations (PSE) are two physics-based methods that, in conjunction with the semi-empirical e^N methods, have exhibited better agreement with experimental data.[1] Disturbance amplification $A/A_0 = e^N$, where A is a disturbance amplitude and A_0 is its initial amplitude before amplification, can be computed for a certain geometry and flow parameters. Transition location is then related empirically to a critical value of N. LST and PSE are important because they enable the extrapolation of limited experimental test conditions to a wider range of cases.

Many transition experiments have been carried out in ground-testing facilities over the past 50 years.[2] One way in which these facilities fail to duplicate flight conditions is the high level of noise that radiates from the turbulent boundary layers normally present on conventional wind tunnel walls.[3] These noise levels are an order of magnitude larger than those observed in flight.[4,5] High noise levels can cause transition to occur an order of magnitude earlier than in flight.[3,5] For instance, $N \approx 5.5$ correlates well with transition location on a sharp cone under noisy flow in multiple facilities.[1] Sharp cones in low-noise facilities typically exhibit transition for $N = 8$–11.[6] Designing experiments with N factors large enough to exhibit natural (as opposed to roughness-induced) transition is difficult in quiet wind tunnels due to the limited maximum Reynolds number (Re) that can be achieved while maintaining laminar nozzle-wall boundary layers.[7]

II. The Boeing/AFOSR Mach-6 Quiet Tunnel

The Boeing/AFOSR Mach-6 Quiet Tunnel (BAM6QT) at Purdue University is presently the only hypersonic quiet tunnel in operation anywhere in the world. In order to minimize complexity and cost, a Ludwieg-tube design was chosen for the BAM6QT. At the time of the compression-cone tests, the quiet-flow run duration was 3–5 s. The tunnel configuration is shown in Figure 1. The maximum stagnation pressure for the BAM6QT is 300 psia (2.0 MPa), although the design maximum quiet pressure is 150 psia (1.0 MPa). While running quietly, the noise level (root-mean-square pitot pressure normalized by stagnation pressure) is less than 0.05%, and it increases to about 3% when noisy.[7]

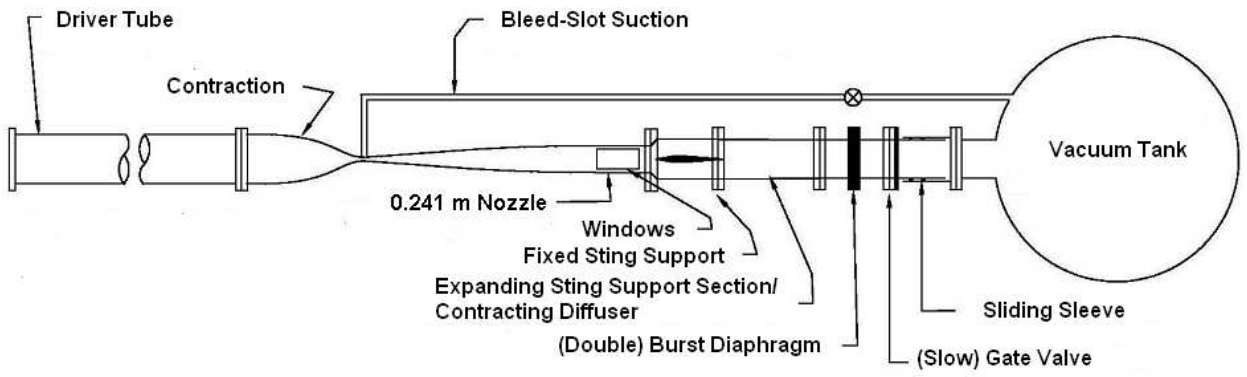

Figure 1: BAM6QT schematic.

The BAM6QT employs many features to maintain laminar nozzle-wall boundary layers, thereby achieving quiet flow.[7] Among these features is a suction slot upstream of the throat that removes the boundary layer on the contraction, allowing a fresh laminar boundary layer to grow on the divergent portion of the nozzle. In order to run quietly, a valve connecting the suction slot to the vacuum tank must be opened. The BAM6QT

can also be run with a noise level comparable to conventional tunnels by leaving the bleed line closed. A more comprehensive discussion of the components of the BAM6QT is contained in Reference 8.

A. Test Section

Figure 2 shows Section 8, the last nozzle section, which doubles as the test section. The region of useful quiet flow lies between the onset of uniform flow and the upstream boundary of acoustic radiation from the onset of turbulence in the nozzle-wall boundary layer. A 7.5° half-angle sharp cone is drawn on the figure. The rectangles are drawn on the nozzle at the location of window openings.

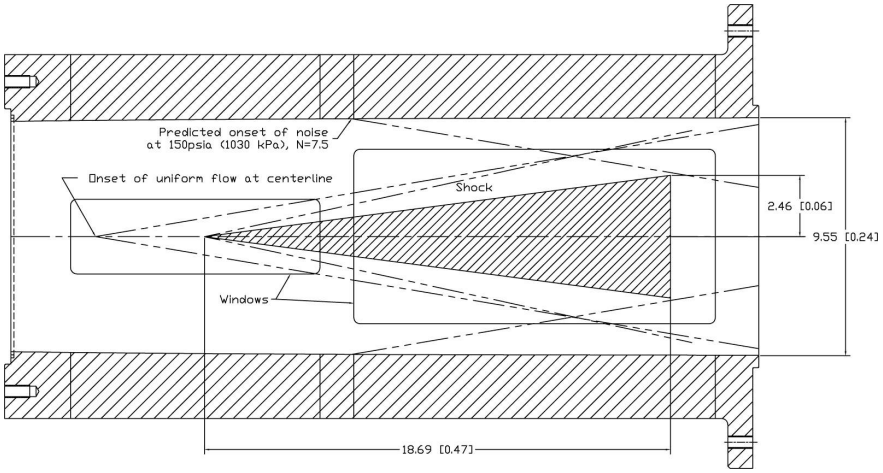

Figure 2: Schematic of the BAM6QT quiet nozzle with 7.5° cone model. Dimensions are inches [meters].

B. Flow Conditions

The stagnation pressure decreases quasi-statically during the run as the expansion wave reflects back-and-forth within the driver tube, dropping to about 70% of its initial value after 5 s.[9] The stagnation temperature at the beginning of each run is nominally 433 K. Like the stagnation pressure, the stagnation temperature decreases quasi-statically during the run to 400 K after 5 seconds.[10]

III. Status of BAM6QT Quiet Flow Performance

Changes in the performance of the BAM6QT have occurred over the past year. Reference 11 reported tunnel performance from January – May 2008. The last few months of 2008 saw an increase in the maximum quiet pressure of the tunnel. The tunnel began running quiet at 153 psia, the maximum allowable working pressure of the large Plexiglas window often used for TSP imaging. In December 2008, porthole windows were installed in the tunnel and a series of eleven higher pressure runs were conducted with initial total pressures between 160 and 180 psia.

The tunnel reached a new record quiet pressure of 163 psia during these tests. Figure 3a shows the total pressure variation during the run as well as a trace from a hot film on the tunnel wall at $z = 74.5$ in. from the throat. A 7° half-angle cone was installed in the tunnel, and the diffuser pipe insert[11] was pushed all the way forward. The initial 0.2 s of the run were before the bleed slots at the throat were opened. When the bleeds opened, the flow immediately became quiet. The rest of the run remained quiet, with occasional turbulent spots passing on the nozzle wall.

Figure 3b shows another run starting at $P_0 = 175$ psia. In this case, the flow initially became quiet at 164 psia. It remained quiet for 0.2 s, then returned to noisy flow for 0.2 s. The flow then oscillated between noisy and quiet flow for over one second before returning to quiet flow below $P_0 = 154$ psia. This was the first and only time this type of oscillation has been seen, and its causes are unknown. Typically, a period of intermittent flow is seen during the transition from noisy to quiet flow, but that intermittency is brief

and occurs at a high frequency. Higher-pressure quiet runs were not attempted again until May 2009. The current quiet pressure remains above 160 psia.

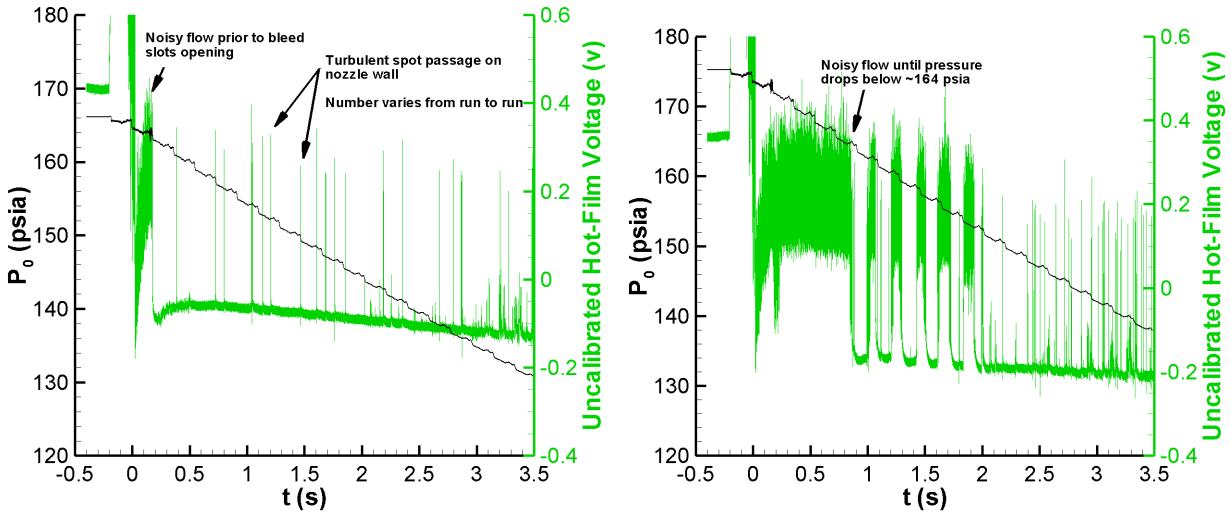

(a) Total pressure and hot-film traces showing new record quiet pressure of 163 psia.

(b) Strange oscillation between noisy and quiet flow.

Figure 3: Tunnel quiet flow tests.

IV. Shutdown Process in Noisy and Quiet Flow

Experiments were performed in October 2008 without a model installed in the tunnel. During the experiments, a difference in the tunnel shutdown process was found depending on whether the tunnel was operated with quiet or noisy flow. The end of the hypersonic portion of the run occurred within a few milliseconds throughout the test section portion of the nozzle during quiet runs. For noisy runs, the shutdown occurred first in the downstream portion of the test section and over one second later in the upstream portion of the test section.

The tunnel shutdown was detected using two different types of sensors mounted on the nozzle wall: hot films and a Kulite pressure transducer. Three hot films were located at tunnel axial coordinates $z = 74.5$, 81.5 and 103.0 in. The two upstream hot films (at $z = 74.5$ and 81.5 in.) were part of a hot-film array mounted on the side of the nozzle wall, described in Reference 12. The downstream hot film ($z = 103.0$ in.) was a Dantec 55R47 paste-on hot film, mounted on the interior of the pipe insert[11] and one inch from its upstream edge. A Kulite pressure transducer, model XCQ-062-15A, was mounted in the nozzle wall at $z = 75.75$ in. to measure static pressure fluctuations. It was oriented parallel to the nozzle wall and flush-mounted with the surface. The Kulite and hot-film sensors were installed both on the lower wall and side wall of the nozzle, however the flow was assumed to be axisymmetric. The end of the hypersonic portion of each run is normally detected with a qualitative analysis of the time trace of the sensors. The shutdown time, or end of hypersonic flow, is characterized by a large change in the sensor mean voltage levels as well as a sudden increase in the root mean square (RMS) voltages.

The shutdown process was observed during two runs at identical conditions. The runs had an initial stagnation pressure of 90–92 psia and were performed with no model installed. The gap between the end of the nozzle and the upstream edge of the pipe insert was closed. In one run, the bleed valves were opened and quiet flow with a laminar boundary layer on the nozzle wall was achieved (Figure 4). In the other run, the bleed valves were closed and the tunnel was operated in conventional noisy mode with a turbulent boundary layer on the nozzle wall (Figure 5). In Figures 4 and 5, the plots on the left show time traces of both the uncalibrated hot film and Kulite voltages. The blue trace is the voltage from the Kulite sensor at $z = 75.75$ in. The plots on the right show the RMS voltages of the hot films, compared to their pre-run values ($t < 0$). The pre-run RMS voltage of the Kulite is not available since the mean level was off the scale

of the oscilloscopes prior to the run. During the quiet run (Figure 4), the shutdown time on all the sensors is 3.6 s, as indicated in both the time traces as well as a sudden increase in the RMS voltages of the hot films. During the noisy run (Figure 5), the shutdown occurs at different times on each sensor. Shutdown is first indicated on the downstream hot film at $z = 103.0$ in. followed by the hot film at $z = 81.5$ in. The shutdown is next indicated on the Kulite at $z = 75.75$ in., and finally on the far upstream hot film at $z = 74.5$ in. Based on these sensors, the shutdown process appears to move slowly upstream for noisy runs, while occurring simultaneously for quiet runs. Table 1 shows the shutdown times indicated on each sensor for the noisy run in Figure 5 as well as an estimation of the propagation speed of the shutdown between sensors. Under noisy flow, the unstarting of the tunnel appears to propagate upstream through the nozzle with a decreasing velocity. No repeat runs have been performed under these conditions.

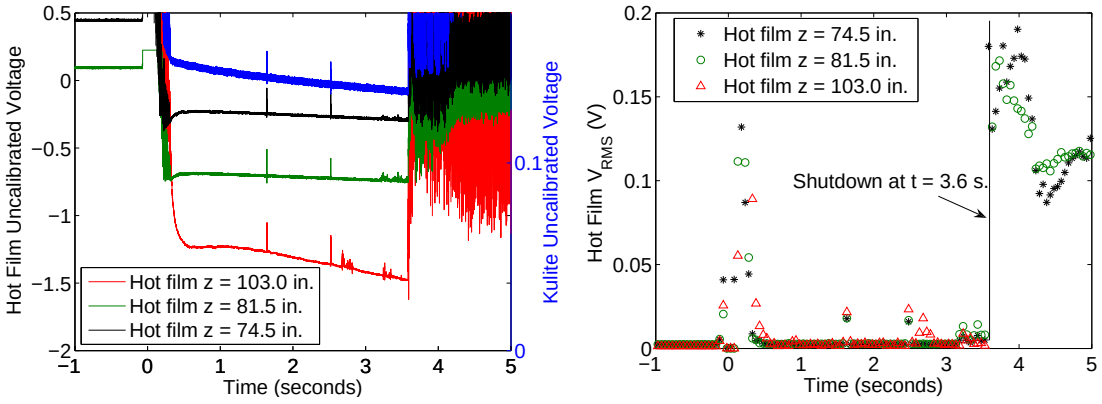

(a) Time trace (b) Hot-Film RMS Voltages

Figure 4: Quiet flow when $P_{0,i} = 90$ psia. Hot films and Kulite sensor show simultaneous shutdown at $t = 3.6$ s.

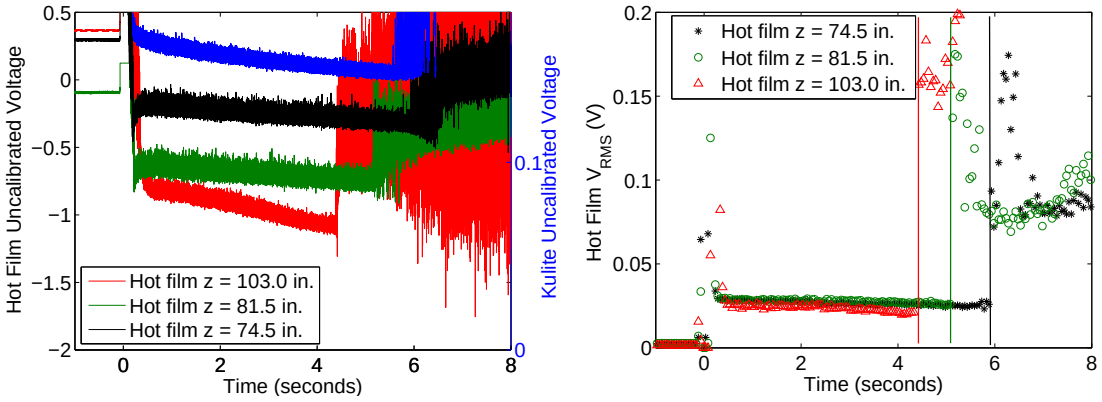

(a) Time trace (b) Hot-Film RMS Voltages

Figure 5: Noisy flow when $P_{0,i} = 90$ psia. Hot films and Kulite sensor show shutdown at different times. The shutdown process appears to be propagating upstream. Colored vertical lines represent the apparent shutdown time indicated by each hot film.

V. Starting of a 3° Blunt Cone in the BAM6QT

A blunt cone was tested in the BAM6QT in an attempt to repeat findings by Müller and Henckel on the effect of nosetip radius on transition.[13] Transition typically moves aft as nosetip radius increases,[2] but Müller saw it move forward with a large enough radius. A 3° half-angle cone was built at Purdue University for the experiment (Figure 6). The frustum of the cone is 65.6 cm in length and has a 9.9-cm base diameter.

Table 1: Shutdown times as indicated on sensors for noisy run.

Sensor	z (in)	Shutdown time (s)	Estimated local shutdown speed (in/s)
Paste-on hot film	103.0	4.4	-
Hot-film array #33	81.5	5.1	31
Flush-mounted Kulite	75.75	5.6	12
Hot-film array #4	74.5	5.9	4

There are three sensor holes at 15-cm spacing along the surface of the frustum. After sensor installation, the access holes (opposite the sensors) were plugged using nylon set screws. Two interchangeable nosetips with 2-mm and 15-mm radii were built. The total length of the cone with the 15-mm nosetip was 67.3 cm.

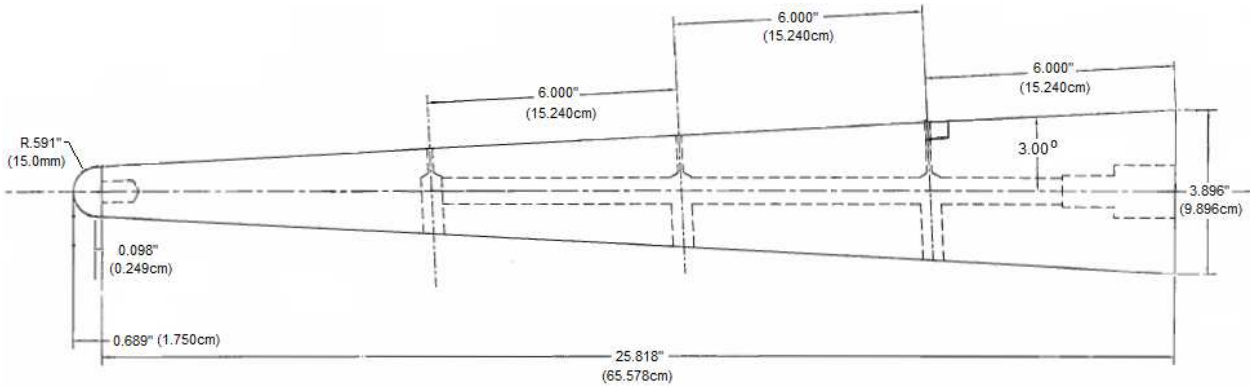

Figure 6: Drawing of 3° blunt cone with 15-mm nosetip.

The cone was first tested to see if the tunnel would start with such a blunt model. The tunnel starting process can be hindered by model blockage as well as the interaction between the cone bow shock and the boundary layer on the tunnel wall.[11] Under quiet-flow conditions, the laminar boundary layer on the nozzle wall is more likely to separate. The adjustable-gap pipe insert was used to attempt to improve starting performance for the 3° blunt cone. A Kulite pressure transducer (model XCQ-062-15A) was installed flush to the frustum surface. This sensor and a Kulite installed on the wall of the diffuser were used to detect if the tunnel had started. An unstarted run was characterized by large unsteady fluctuations on both the cone and diffuser Kulites. A started run was characterized by a smooth voltage trace on both sensors.

The cone was tested with the 2-mm-radius nosetip at 0° angle of attack at $P_0 = 40$–250 psia under both noisy and quiet flow conditions. There was no gap between the pipe insert and the end of the nozzle. Under these conditions, the cone always started.

The starting performance when using the 15-mm nosetip was of greater concern. The effect of the 15-mm nosetip on starting performance was tested with the cone at 0° and 2° angle of attack. The pipe insert gap was varied between 0 (no gap), 0.75, and 1.5 in. The initial stagnation pressure of the tunnel was varied under both noisy and quiet flow conditions. Results showed that the cone with the 15-mm nosetip always started in the BAM6QT at 2° angle of attack. These tests were done at $P_0 = 45$–92 psia under noisy and quiet flow. Tests at 0° angle of attack with the 15-mm nosetip revealed that the cone only started with a gap present in the pipe insert. The cone started for gap distances of both 0.75 and 1.5 in. under quiet and noisy flow for $P_0 = 45$–220 psia. The cone (with 15-mm nosetip) never started when the pipe insert gap was closed. Transition data have not yet been obtained due to difficulties using the temperature-sensitive paint.

VI. Pipe Insert Extension Design and Installation

New sting-support and diffuser sections were installed in late 2007 in an attempt to start larger blunt models. Reference 11 provides a description of the design and testing of the new sections. In contrast to the old sting-support section, which had a constant 9.5-in. diameter, the new section features a 45° expansion from 9.5 in. to a 14.125-in. diameter just downstream of the nozzle exit. The new configuration resulted in a nearly 50% decrease in run time and showed no significant improvement in starting performance.[11]

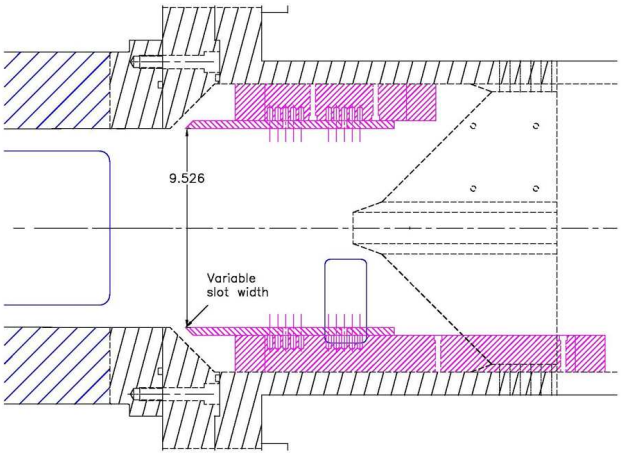

Figure 7: Schematic of steel straight-pipe insert in new sting-support section.[11] Dimensions in inches.

A straight, stainless-steel pipe insert of the same diameter of the nozzle exit was later installed.[11] The insert, shown in Figure 7, is mounted just downstream of the nozzle and can be repositioned to form a slot between it and the nozzle exit. The annular region outside of the insert was expected to be at a lower pressure than the main flow, resulting in suction in the slot. By adjusting the slot width, it was believed that the upstream boundary layer could be removed to better promote attached flow. Preliminary testing again showed no significant improvement in starting performance.[11]

In an effort to increase run times and utilize the new sting-support section to start larger blunt models, an extension to the pipe insert was designed. Figure 8 shows a model of the pipe insert extension installed in the sting-support and diffuser sections. The extension consists of six interlocking cylinders, a total of 8 ft in length, with a constant 9.5-in. inner diameter equal to that of the nozzle exit. The extension spans from the downstream end of the steel pipe insert to the downstream end of the diffuser and is supported coaxially by a set of rails bolted to the diffuser. The sections were machined from cast XHA Nylon. XHA Nylon was chosen for its high tensile strength (necessary to withstand tunnel starting loads) and relatively low machining cost.

As with the pipe insert, the streamwise location of the extension can be adjusted to any of 5 positions at increments of 0.375 in. This allows for slots upstream and downstream of the pipe insert, a single slot upstream of the pipe insert, or no slot. The effect of suction through the slot on shock/boundary layer interactions, as well as optimal slot width, will be determined by varying the pipe insert and extension positions. With no slot between the extension and the pipe insert or the insert and the nozzle exit, the extension mimics the old constant-diameter diffuser and sting-support sections. With this setup, longer run times similar to the old configuration can potentially be achieved because of the increased efficiency of the diffuser. The extension's segmented design also allows for flexibility in testing future inserts. For example, alternative methods of controlling shock/boundary layer interactions, such as porous walls and ramp inserts, may be tested by substituting sections of the extension. Figure 9 shows the extension in the tunnel after installation in April 2009. The XHA Nylon has thus far withstood all starting and shutdown loads. Results from preliminary runs show a nearly 50% increase in run time under quiet flow. Further investigation is needed to determine the exact effect on run time as well as any benefits to starting larger blunt models.

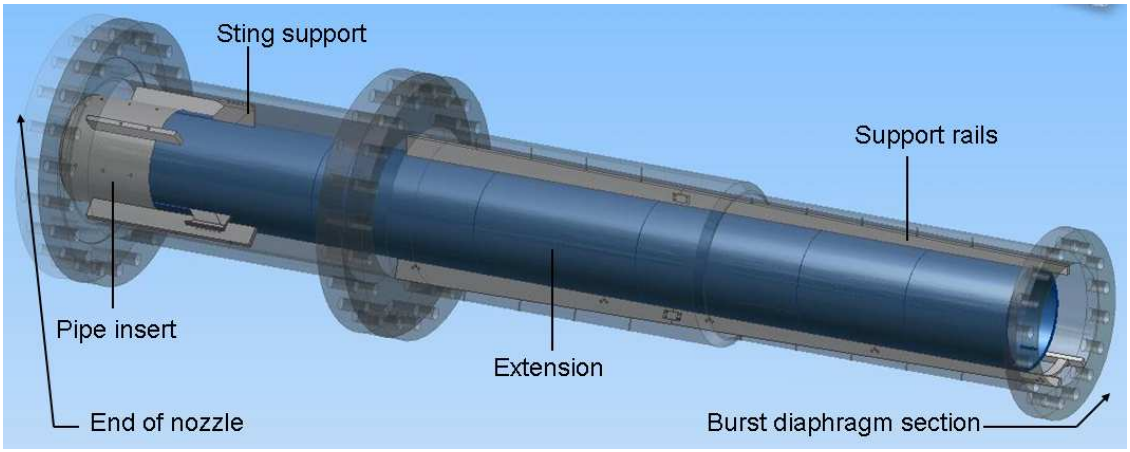

Figure 8: New constant-diameter pipe insert extension (dark blue) installed in the sting-support and diffuser sections (transparent).

(a) View looking downstream

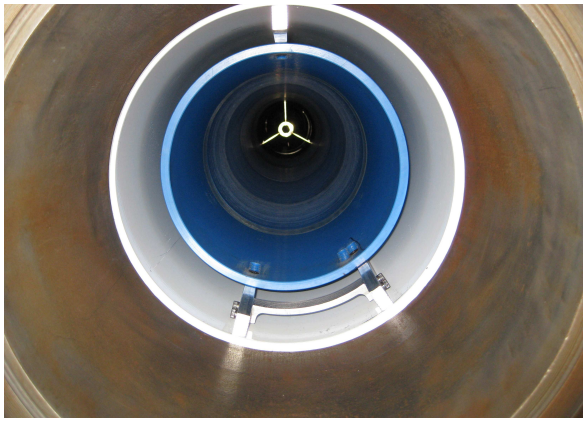

(b) View looking upstream

Figure 9: (a) View looking downstream from the nozzle exit. The blue extension meets at the downstream end of the stainless-steel pipe insert, ahead of the sting support. (b) View looking upstream from the burst diaphragm section. The extension is secured coaxially on three rails spanning the length of the diffuser. The back of the sting support is visible far upstream.

VII. Design of a Compression Cone using STABL

Johnson et al. conceived a plan to optimize parametrically-defined geometries to achieve maximum or minimum boundary-layer stability.[14] Among their results was an axisymmetric surface defined by a Bezier curve that achieved maximum N factors of approximately twice those of a baseline 7° half-angle cone with small bluntness. This success suggested that a properly-designed model could exhibit a high enough N factor to exhibit natural transition in a facility such as the Boeing/AFOSR Mach-6 Quiet Tunnel (BAM6QT).

At Purdue University, the Stability and Transition Analysis for hypersonic Boundary Layers (STABL) software suite[15] was used to calculate mean flow and stability for a family of compression cones in order to find a design that exhibited the highest possible N factor. A model of this optimal design was then built and tested in the BAM6QT (see section VIII).

A. Initial Computations to Choose Design

A flared cone geometry was desired with large N factors that would cause transition under quiet-flow conditions. A compression geometry was expected to cause transition due to an adverse pressure gradient acting along the body. In addition, the ideal geometry would have a constant-thickness boundary layer resulting in continuous amplification of a narrow range of instability frequencies.

For simplicity, a family of circular-arc geometries were chosen for study. A similar study was performed using parabolic geometries, however the results were comparable and will not be reported here. The body of the circular-arc geometry resembles a cone, but with a concave surface. MATLAB was used to create geometry coordinates for STABL, which was then used to generate the grid.

1. Geometry Generation

Previous work by Johnson et al. used an optimization algorithm to find the geometry that resulted in the largest N factors.[14] In this study, each test case was run manually using STABL. Very few cases could be completed due to time constraints. For this reason, two variable parameters were chosen to describe the geometry and the other parameters were held constant. The two independent parameters were the initial half-angle of the nose and the radius of curvature of the body. These two parameters were varied to create the geometries for the study, and an ideal geometry for building the compression cone was selected based on the results. The nose radius was set as a constant 1 mm for two reasons: (1) easier grid generation and (2) a blunt nose was desired for machining purposes. In order to ensure that the model would start in the BAM6QT, the base diameter was constrained to a constant 0.1 m to match typical cone models. The model length depended on the two independent parameters and varied from approximately 0.28–0.45 m (11–18 in.), which matches typical model lengths in the BAM6QT.

Computational grid generation started with fifty evenly-spaced points on the nose. The body coordinates were created such that the specified nose half-angle was obtained at the mating location. The slope was continuous at the mating location between the nose and body points. The distance between the first two points of the body was set equal to the nose point spacing. A "stretching factor" was introduced to the MATLAB code, such that the distance between consecutive points along the body was multiplied by this factor. A stretching factor of 1.017 was used for the geometries in the initial study, resulting in around 360 total points for each geometry. The maximum distance between streamwise points was below 6.5 mm at the aft end of the cone.

2. Conditions for Computations

The circular-arc geometries were run in conditions simulating the Boeing/AFOSR Mach-6 Quiet Tunnel at a stagnation pressure of 140 psia (near the maximum quiet stagnation pressure). The angle of attack was zero degrees and the flow was axisymmetric. A summary of the conditions used for the simulation appears in Table 2. In order to decrease the computation time, a perfect gas was assumed. Since the static temperature in the BAM6QT is near 53 K, a perfect gas assumption was deemed valid. Chemical vibration was turned off. The STABL "non-reacting air" chemistry model was used. Room temperature was used as the isothermal wall boundary condition. All computations were performed on a 3.06 GHz dual-core Linux machine with 2 GB of RAM.

Table 2: Simulated conditions of the Purdue Mach-6 Quiet Tunnel.

M_∞	P_0 (psia)	T_0 (K)	T_∞ (K)	ρ_∞ ($\frac{kg}{m^3}$)	T_{wall} (K)	Chemistry	Vibration
6.0	140	433	52.8	0.0403	300	Non-Reacting Air	Off

3. Coarse Grid Generation and Initial Solution

A coarse grid was generated using the STABL grid generation module. The "lower shape power law upper" grid generation setting was used. In the "lower shape power law upper" grid definitions, the lower shape (body) is defined with an external file consisting of the x and y coordinates. The upper surface of the grid is defined by an ellipse near the nose and a power-law grid border. The power-law grid border is altered by changing the angle at which the border intersects with the nose ellipse as well as the power law exponent, which alters the curvature of the upper surface of the grid. Two hundred body-normal points were used in the coarse grid with a spacing factor of 0.9 to give slight clustering near the surface. Two hundred vertical points were chosen for faster convergence while still resolving the location of the shock. A coarse grid was created such that the shock shape would be enclosed within the grid. The CFD solver was run for 3500 iterations at CFL numbers less than 50, long enough for the shock shape to become resolved. The coarse-grid CFD solution was then used to create a shock-tailored grid, to be used for mean flow analysis.

4. Grid Tailoring and Mean Flow Solution

The built-in "grid tailoring" module was used to create a shock-tailored grid from the initial coarse-grid CFD solution. The grid tailoring module allows the STABL user to specify the number of body-normal points and add stretching in the body-normal direction (to cluster points within the boundary layer). Reference 16 recommended as a rule-of-thumb that the boundary layer consist of at least 100 body-normal points. A total of 368 body-normal points were chosen for the tailored grid. The grid tailoring module was used to examine the coarse grid, detect the shock location, and create a grid that was tailored to the shock. STABL detected the shock location where there was a 0.5% change in Mach number from the freestream value. Figure 10 shows sample grid tailoring results near the nose of the geometry. The red line shows the borders of the initial coarse grid which encloses the shock. The black contour lines represent Mach number contours from the final CFD solution, and are used to show the shock location. The green line shows the shock-tailored grid enclosing the shock. There were 10 points outside of the shock.

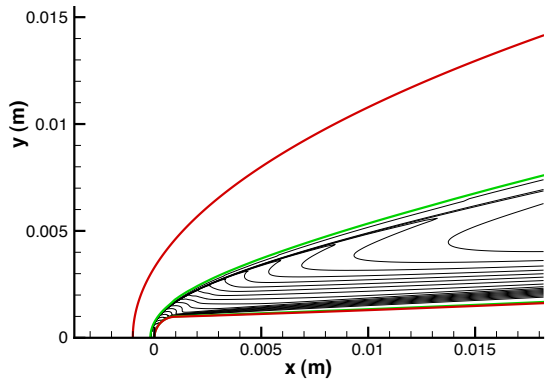

Figure 10: Sample coarse grid and tailored grid. Mach number contours are shown in black. The red line is the border of the initial coarse grid. The green line is the border of the shock-tailored grid.

After completing the mean flow solution, the results were checked to ensure accurate stability calculations would be possible. The number of body-normal grid points within the boundary layer was 100 or greater for all cases. The boundary-layer edge location was detected by STABL and was defined as the location where the total enthalpy reached 99.5% of its freestream value. It is recommended that the dimensionless wall parameter y^+_{wall} be less than unity,[16] and the value of this parameter was verified for all cases.

5. *Stability Analysis using PSE-Chem*

When an appropriate mean flow solution was obtained, a stability analysis was performed using the parabolized stability equation solver in STABL (PSE-Chem). More information about the PSE-Chem code can be found in Reference 15. To be consistent with the mean flow, chemistry and vibrational modes were turned off. The stability analysis was performed in two steps. First, test matrices consisting of arc length values and frequencies were defined in an initial coarse stability grid. The coarse grid calculations were used to identify regions of interest as well as initial N factor estimation. Then, a region of interest was found and the stability analysis was re-run with a fine grid placed over that region.

Figure 11a shows an example of an initial coarse stability diagram with the test matrices shown. The small yellow test matrix was an auto-refined matrix added by STABL to the beginning of the instability region. From the coarse stability diagram, a region of positive amplification was identified and a fine stability matrix placed over it. Figure 11b shows increased resolution in the region of interest as a result of the additional test matrix.

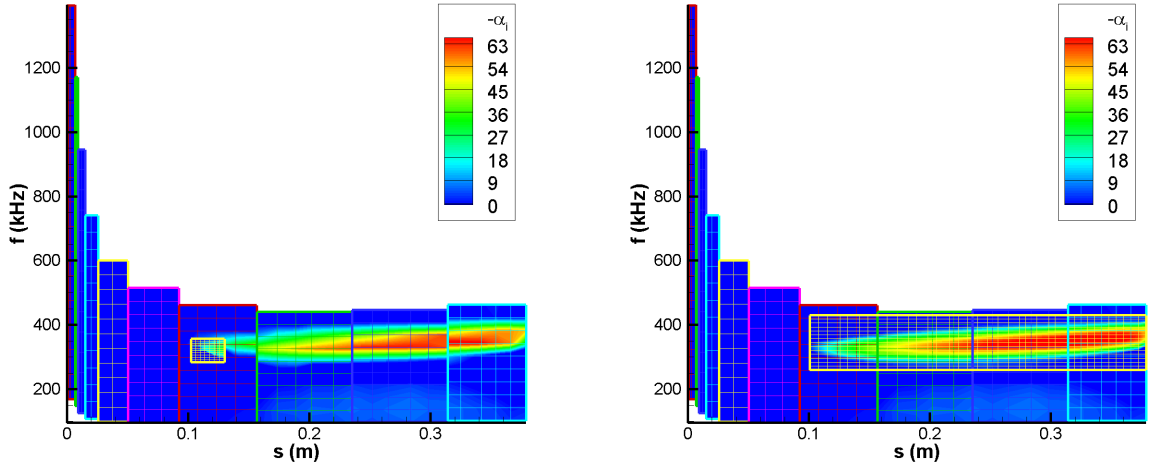

(a) Initial stability grid.

(b) Fine grid placed over region of interest.

Figure 11: Example coarse and refined stability matrices.

6. *Selection of Final Compression Cone Design*

Five geometries were analyzed and are summarized in Table 3. The frequencies are larger and the N factors are lower than those obtained in preliminary calculations. Computations by Balakumar were performed for similar conditions using a different code.[17] A discrepancy was seen between the computational results. After further investigation, using different settings in the PSE marching procedure in PSE-Chem produced better agreement between the two results.

Case 1 served as the baseline case and its parameters were randomly chosen. Cases 2 and 3 examined the effect of the curvature of the body, while Cases 4 and 5 examined the effect of the nose half-angle. All cases except for Case 3 featured a nearly-constant-thickness boundary layer along the body and a small range of instability frequencies that were amplified continuously along the body. The "maximum N factor" was defined as the N factor at the aft end of each cone, while f_{unstable} was defined as the frequency that was most amplified at the end of the cone. For all cases except for Case 3, this frequency was most amplified along a large portion of the body. Case 2 was selected as the final compression cone design because it had the lowest unstable frequency of around 285 kHz and the highest maximum N factor. A lower frequency was desired to measure second-mode waves using fast pressure sensors. The final compression cone design had a radius of curvature of 3 m and an initial nose half-angle of 2.0°.

Table 3: Summary of initial results. R is the radius of curvature of the body, θ_i is the initial nose half-angle, L is the cone length, and f_{unstable} is the most amplified disturbance frequency at the end of the cone (from the PSE results).

Case	Description	R (m)	θ_i (deg)	L (m)	f_{unstable} (kHz)	Maximum N factor
1	Baseline	2	2.0	0.38	340	15.0
2	Larger R	3	2.0	0.45	285	16.4
3	Smaller R	1	2.0	0.28	513	9.5
4	Smaller θ_i	2	1.0	0.42	331	14.7
5	Larger θ_i	2	3.5	0.32	366	14.2

B. STABL Compression Cone Results

After the compression cone model was manufactured, new STABL results were generated with a finer mean-flow grid. A total of 644 streamwise points was generated by changing the stretching factor to 1.008. The maximum spacing between streamwise points was decreased from 6.5 mm to 3.5 mm at the aft end of the cone. The mean flow and PSE results were computed using the same methods described earlier, and were comparable to results from the initial study. Additional analysis was performed by Christopher Alba.

1. Mean-Flow Results

Mean-flow contour plots of the density and Mach number are shown in Figures 12a and 12b, respectively. Though the stability analysis of the compression cone was the primary focus of this experiment, the mean flow highlights the important flow features. The shock locations were found from large changes in density and Mach number. There appeared to be a bow shock and a large recompression region. The shock was roughly elliptic in shape at the nose and curved in toward the body farther downstream, but did not impinge upon it. Downstream of the shock, the flow was expanded into a low-density region. A recompression region appeared to begin at or before $x = 0.1$ m, which is where STABL predicted that the boundary-layer disturbances began growing.

2. LST Results

The Linear Stability Theory (LST) stability diagram shows a region of amplification starting at an arc length of 0.1 m (Figure 13a). Only axisymmetric waves were analyzed since these are the most unstable second-mode disturbances.[18] The bandwidth of the amplification region is about 100 kHz, ranging from 250–350 kHz. Disturbances of $f = 279$ kHz are the most amplified, with growth rates of around 60/m. Though STABL does not automatically compute N factors from LST results, the growth rate data from the LST diagram were used to compute N factor curves. The LST results predict an N factor of 16 at the aft end of the cone for $f = 279$ kHz (Figure 13b). The N factor used for transition correlation is normally taken from an envelope of multiple N factor curves, however in this case one curve defines the envelope. The LST stability diagram is plotted using s, the surface arc length, as a default in STABL. The LST N factors are plotted using x, the body axial coordinate, for easier comparison to the experiments. On the compression cone, however, the half-angle of the cone is low so that $s \approx x$.

3. PSE Results

The PSE results from the STABL computations are shown in Figure 14. Several N factor curves from the most-amplified frequencies are shown, with each curve showing increasing N factors along the body of the cone. The most-amplified curve at the aft end of the cone was $f = 286$ kHz, which was similar to that from the preliminary study results (Case 2 in Table 3). The maximum N factor from the PSE results was near 16 at the aft end of the cone. The PSE results show maximum growth rates of 60/m (Figure 14b).

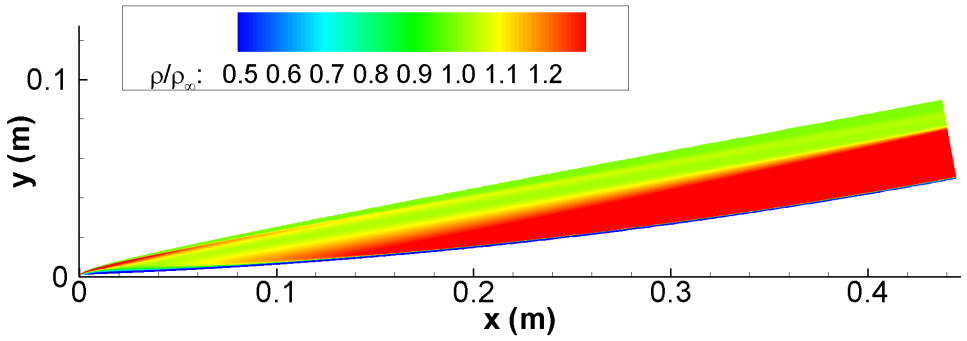

(a) Nondimensional density $\frac{\rho}{\rho_\infty}$.

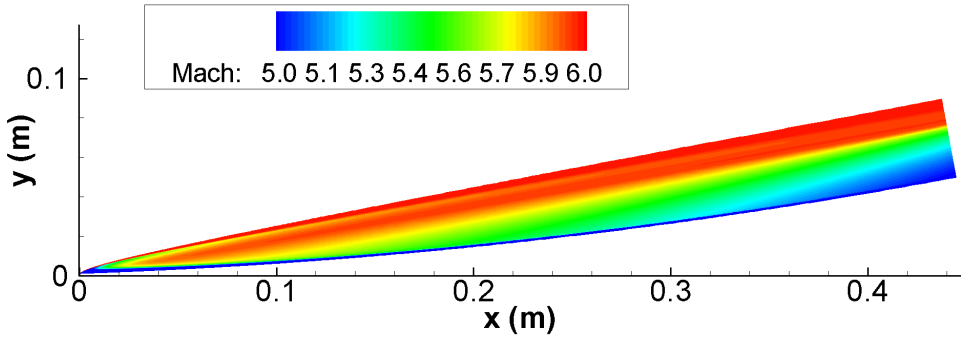

(b) Mach number.

Figure 12: Mean flow contour plots.

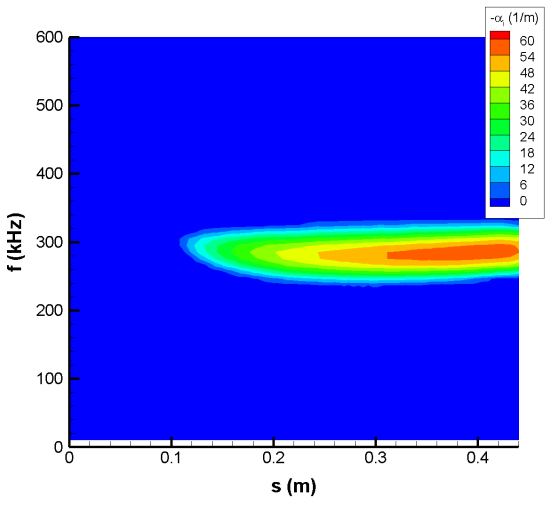

(a) LST stability diagram

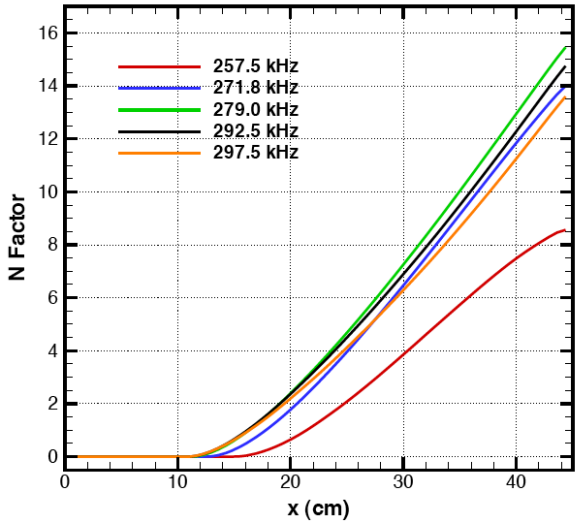

(b) N factors from stability diagram.

Figure 13: LST results for the compression cone.

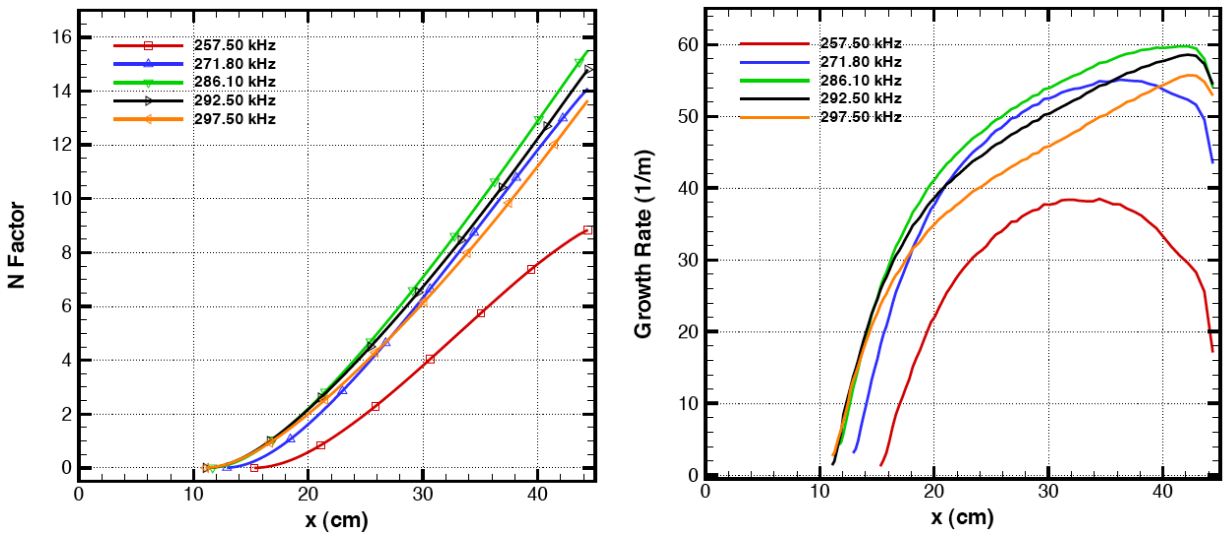

(a) PSE N factors.

(b) PSE growth rates.

Figure 14: PSE results for the compression cone.

VIII. Instability Measurements on the Compression Cone

A. Model Design and Fabrication

The compression cone model was fabricated by the Purdue University Aerospace Sciences Laboratory machine shop. It consists of two parts: a 142-mm-long 17–4 PH H1150 stainless-steel nosetip and a 303-mm-long 6061 T6 aluminum frustum (Figure 15). The blunt nosetip has a 1-mm radius. The cone diameter is 18.5 mm at the joint and 99.5 mm at the base. Three holes for 3.18-mm- (1/8-in.-)diameter sensors are located at $x = 0.2$, 0.3, and 0.4 m. The centers of the sensor holes are normal to the surface contour.

B. PCB Fast Pressure Sensors

Measurements of second-mode waves under quiet conditions in hypersonic tunnels have typically been made using hot wires. Hot-wires have the high frequency response needed to measure second-mode instabilities.[19] However, hot wires are single-point sensors and cannot measure multiple points along the same streamline simultaneously. They must be physically inserted in the flow and frequently break. Successful measurements have recently been made with PCB fast pressure sensors in multiple tunnels, under both noisy and quiet conditions.[20–23] These sensors are robust and require no protrusion into the flow. Using several sensors, multiple streamwise positions can be measured simultaneously with no downstream influence. PCB132A31 sensors are piezoelectric pressure transducers with a high frequency response. They have a resonant frequency of over 1 MHz. The signal from the sensors is high-pass filtered to measure pressure fluctuations above 11 kHz. Mean pressure measurements are not possible since the PCB sensors are AC coupled. They are capable of measuring fluctuations as large as 50 psi with a resolution of 1×10^{-3} psi.[24] The sensing area of the PCB sensors is a 1 mm $\times$ 1.6 mm rectangle. The orientation of the rectangle with respect to the flow direction was not controlled, so there is some uncertainty in the spatial resolution for each sensor.

The PCB sensors were installed in the compression cone model to attempt to measure instability-wave frequencies and amplitudes. The sensors were installed at $x = 0.2$, 0.3, and 0.4 m. The step between the sensor and the model surface ranged from 30–80 μm and was measured using a Mitutoyo surface roughness tester. The spatial resolution of the sensors remains a concern as the sensing area was large when compared to the predicted second-mode wavelength of 1.8 mm (0.07 in). This effect remains to be quantified. In addition, the sensors were designed as time-of-arrival sensors and have not yet been dynamically calibrated for the high frequency and low amplitude of second-mode waves. In the absence of a dynamic calibration, the factory calibration was used to estimate pressure fluctuation magnitudes.

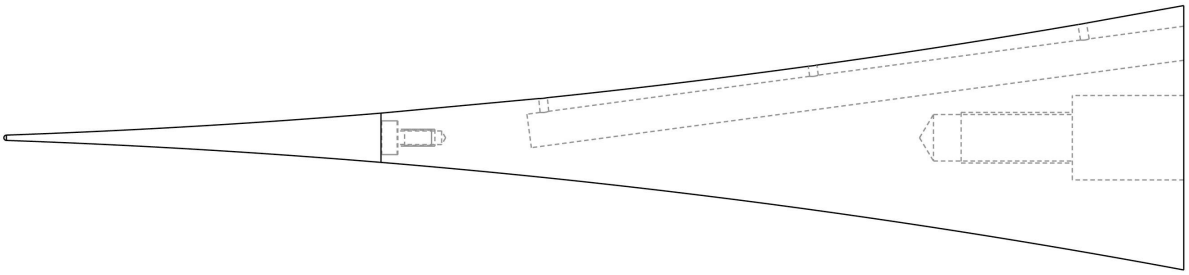

(a) Drawing.

(b) Photograph with sensor holes visible. A 6-in.-long scale is shown for reference.

Figure 15: Compression cone model.

C. Data Acquisition

Data were acquired using two DPO7054 series Tektronix Digital Phosphor Oscilloscopes. Data for PCB sensors were acquired for 10 s with a sampling rate of 2 MHz using Hi-Res mode. Data from 1 s before the run began were recorded for comparison to the flow-on pressure fluctuations. A contraction Kulite sensor was used to determine tunnel stagnation pressure. Two Senflex hot-films were used in conjunction with a Bruhn constant temperature anemometer to determine the length of the run as well as to qualitatively determine whether the flow was quiet or noisy.

D. Data Analysis Method

Power spectra were computed using MATLAB. Signal samples lasting 0.1 s were analyzed using a Welch method of spectrum estimation with at least 900-point Blackman windows and 50% overlap. A total of 500 FFTs were averaged. Because the PCB sensors cannot measure mean pressure, the mean surface pressure from computations was used to normalize the measured pressure fluctuations. Additional mean-flow computations were performed at stagnation pressures of 40 and 90 psia. At each sensor location (for all computed cases) the ratio of static pressure to stagnation pressure was constant. The pressure fluctuation level P'/P_{mean} was found by integrating over the frequency band of each peak in the power spectra.

E. Results

The tunnel stagnation pressure was varied and tests were performed under both noisy and quiet flow conditions. To check flow symmetry, the cone was rotated so that the PCB sensors would measure the waves at different angular positions. The rotation angle showed no noticeable effect on the frequency or amplitude of the waves.

1. Second-Mode Instability Waves under Quiet Flow

Several runs with various initial stagnation pressures were performed under quiet flow conditions and large-amplitude peaks were seen in the power spectra of the PCB sensor signals. Figure 16 shows spectra from several different runs using the same sensor at $x = 0.4$ m. As stagnation pressure (and Reynolds number) increased, both the frequency and amplitude of the peaks increased. Between $P_0 = 90$–140 psia, the peak frequency shifts from 230–290 kHz. The peak fluctuation levels grow from 0.2% to 5% of the mean. The Reynolds-number dependence of the peak frequency suggests that the peaks were instability waves. The peak amplitudes were noticeably greater than the baseline noise. At $P_0 = 138.8$ psia, the fluctuation levels of the peak at 290 kHz were 5% of the mean. In addition, a harmonic peak was visible at the largest Reynolds number suggesting the presence of nonlinear effects. At high stagnation pressures under quiet flow, the high-frequency waves were large enough to be visible on the signal time trace (Figure 17).

At each axial station, the results were compared to the most-amplified frequency in the computations. The shape and width of the measured peaks are shown in Figure 18. N factor data from the computations at 140 psia are plotted for comparison. A comparison between the measured and computed peak frequencies is shown in Table 4. The experimental and computed frequencies agree to within 2.8–3.5%. The lack of transitional features such as frequency broadening, however, indicate that at N factors of 13 the flow is still laminar.[22] The sensors did not show the expected wave growth, perhaps due to the averaging problems. The fluctuation amplitude P'/P_{mean} decreased between sensors. Transition was never observed under quiet flow, even at $P_0 = 160$ psia where the maximum N factor would be higher than 13.

Position x **(m)**	**Computed Freq. Peak (kHz)**	**Measured Freq. Peak(kHz)**	**Percent Diff. in Freq.**	**Comp.** N **Factor**	**Meas.** P'/P_{mean}
0.2	287	294.9	2.8%	2.2	0.084
0.3	285	293.0	2.8%	7.2	0.061
0.4	285	294.9	3.5%	13	0.055

Table 4: Computed and measured peak values for waves at the three sensor stations in Figure 18.

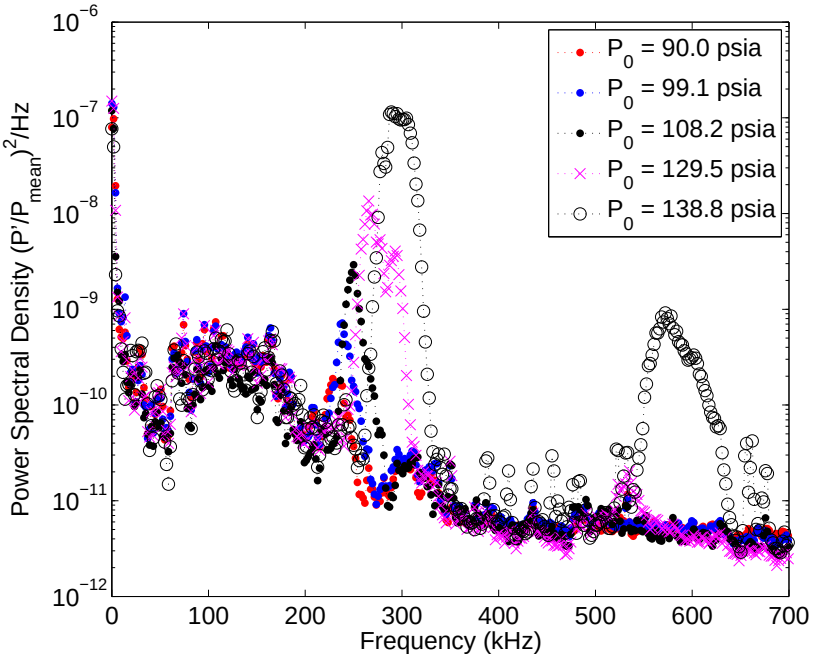

Figure 16: PCB data from several quiet runs at $x = 0.4$ m, showing linear and nonlinear growth. Note the second harmonic at high pressure.

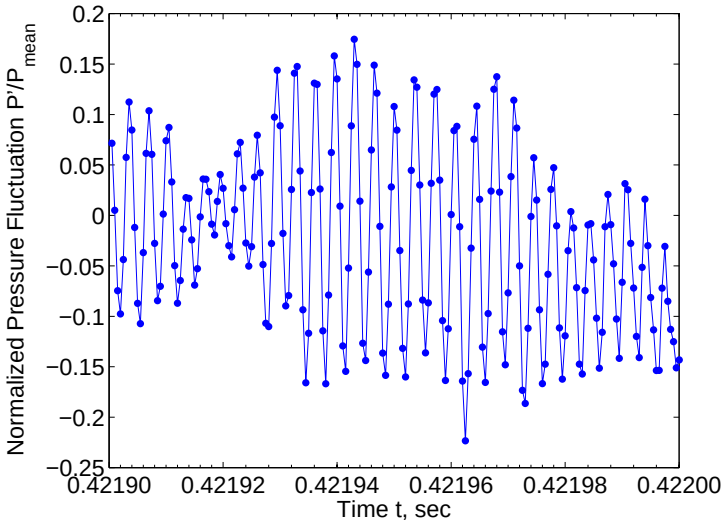

Figure 17: Time trace showing second-mode waves. $P_0 = 138.8$ psia, quiet flow, $x = 0.2$ m.

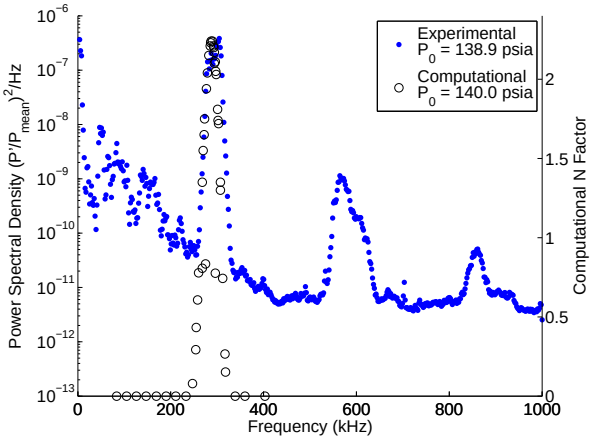

(a) x = 0.2 m, quiet flow

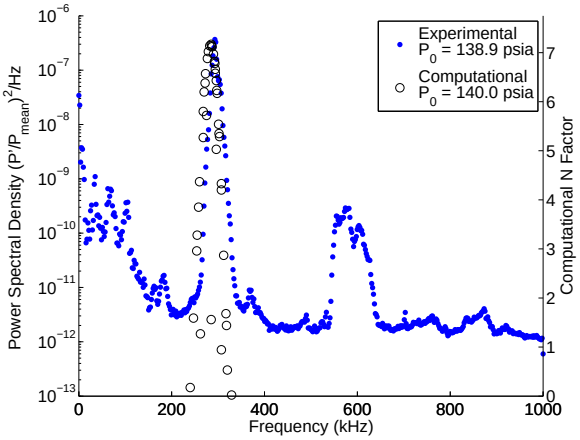

(b) x = 0.3 m, quiet flow

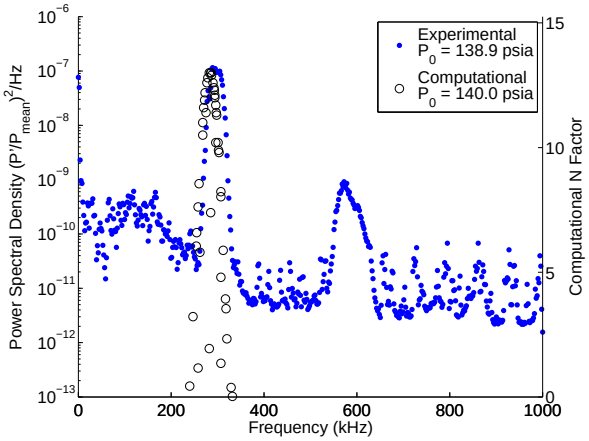

(c) x = 0.4 m, quiet flow

Figure 18: Comparison of measured spectra for $P_0 = 140$ psia (quiet flow) with computed N-factor vs. frequency.

2. *Instability Waves and Transition under Noisy Flow*

Though transition was not observed under quiet flow, it was seen during noisy runs at similar stagnation pressures. Figure 19 shows power spectra from the three sensors during a single noisy run at $P_0 = 137.5$ psia. The sensor at $x = 0.2$ m shows a peak near 290 kHz, the frequency at which waves were seen under quiet flow. The pressure-fluctuation levels at $x = 0.2$ m were higher than seen under quiet flow, and the peak was less pronounced. At $x = 0.3$ m, broadening of the 290 kHz peak can be seen and the broadband noise levels were higher. Due to the presence of a peak in the spectra at $x = 0.3$ m, it remains unclear if the flow was transitional or turbulent. At this location, $N \approx 7$, so turbulent flow may or may not be expected under noisy flow conditions. At $x = 0.4$ m, the flow appeared to be turbulent. There was no peak present and the broadband noise levels were higher. At $x = 0.4$ m, $N \approx 13$, so turbulent flow would be expected for noisy conditions.

Noisy-flow data from a single sensor at $x = 0.4$ m at various stagnation pressures are compared in Figure 20. As the stagnation pressure (and Reynolds number) were increased, the broadband noise rose to high levels, then fell again. The flow at $P_0 = 40$ psia was thought to be laminar. At $P_0 = 72.9$ and 91.2 psia, the fluctuation levels increased and a peak was present. The high fluctuation levels indicated that the flow may be transitional, but with the presence of a peak may not be turbulent. The flow at $P_0 = 138.2$ psia had no peak and appeared to be turbulent, though the pressure fluctuation levels were lower than those at lower Reynolds number. When using PCB sensors on a straight cone, Casper et al. observed that fluctuation amplitudes may be lower for turbulent flow than for transitional flow.[22]

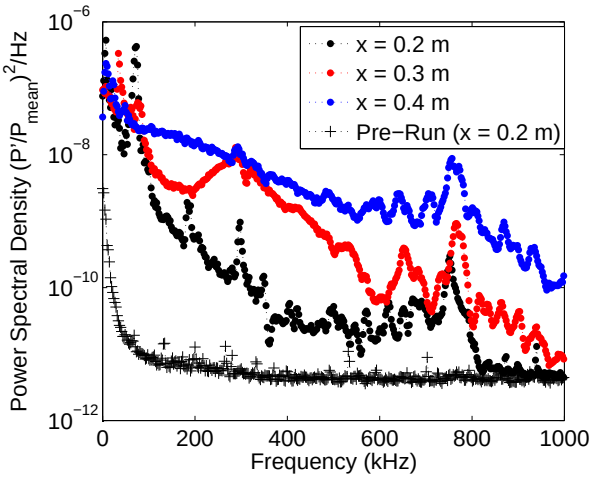

Figure 19: PCB data from a single noisy run, showing frequency broadening and turbulence. $P_0 = 137.5$ psia.

3. *Problems with PCB Measurements*

Several problems were noted in using PCB sensors to measure instability waves and transition. As shown in Figure 21, one sensor failed to detect waves when they were clearly visible on the other two sensors. The sensor detected waves at times, but only at high Reynolds numbers and generally showed a smaller amplitude than the other two. The sensor was more recessed than the two other sensors by about 10 μm. This created a cavity over the sensor, the effect of which is uncertain. It is possible that some PCB sensors are not useful for detecting second-mode waves, due to manufacturing variations. There is no previous record of such a problem, but the sensors were not designed to measure instability waves. Two sensors were replaced during testing. Two new sensors were selected that had calibration values similar to those of the other sensors. This method of selection may also increase consistency in the measurement of wave amplitudes between the three sensor positions.

Growth of the waves with increasing downstream position was hardly ever observed under quiet flow. A steady amplitude, or even attenuation, was often seen (Figure 22). The poor spatial resolution of the sensors may prohibit accurate detection of fluctuation amplitudes for this case. The computations showed the boundary layer thickness as about 0.9 mm over most of the cone at a stagnation pressure of 140 psia. The

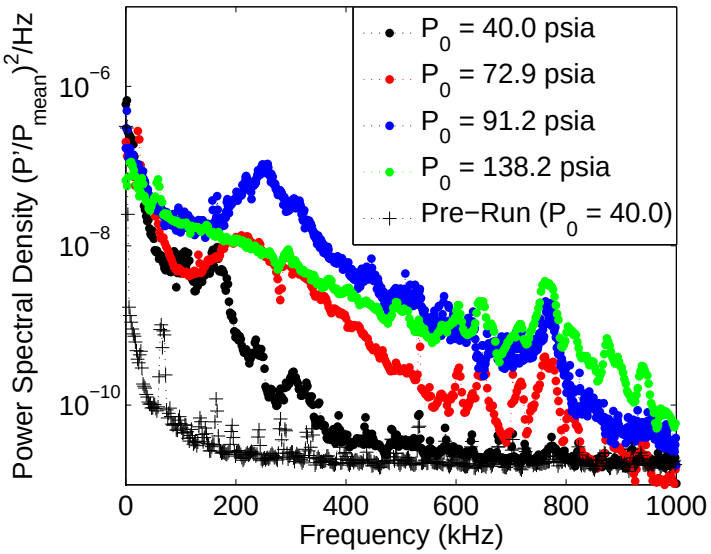

Figure 20: Effect of Reynolds number on spectra at $x = 0.4$ m under noisy flow conditions.

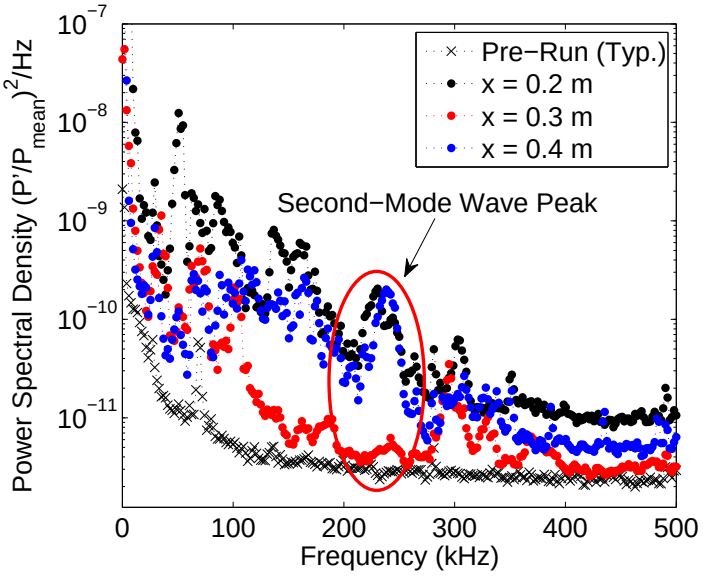

Figure 21: Inconsistency detecting waves under quiet flow. The sensor at $x = 0.3$ m did not detect waves, while the other two sensors detected waves at a similar frequency. $P_0 = 89.5$ psia.

second-mode wavelength can be roughly estimated as about 1.8 mm, or twice the boundary layer thickness. The sensing area is 1 mm × 1.6 mm, which is 0.6–0.9 times the second-mode wavelength. Averaging of the instability waves may have occurred due to this poor spatial resolution.

The lack of increasing wave amplitude along the axial direction of the cone could also indicate that the wave amplitudes actually remained constant, though this seems unlikely. Without the use of a different instrument for measuring the waves, it is impossible to interpret the amplitudes and thus wave growth. Measurements from different axial positions using the same sensor are compared at the same freestream Reynolds number in Figure 23. There still does not appear to be growth with increasing downstream position, indicating that consistency between sensors might not be the problem. The PCB sensor data showed that large second-mode instability waves can be detected, but uncertainties in the fluctuation amplitude remains to be resolved.

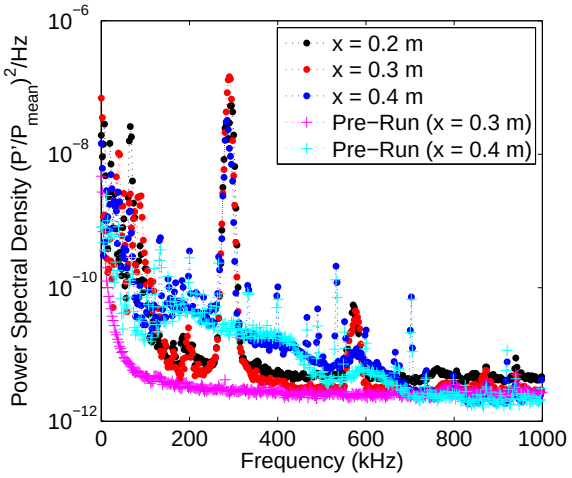

(a) No growth with downstream position. Quiet run, P_0 = 142.5 psia, all axial stations.

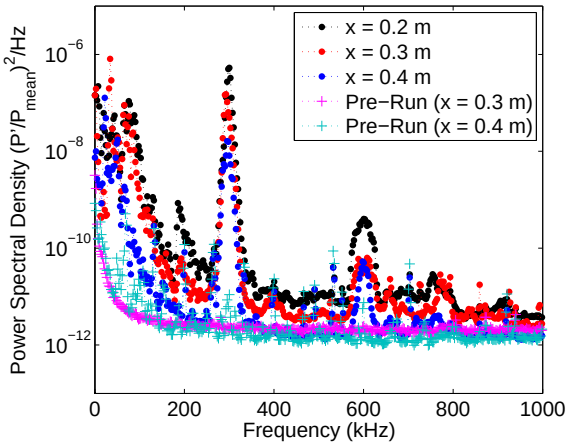

(b) Attenuation with downstream position. Quiet run, P_0 = 149.7 psia, all axial stations.

Figure 22: Lack of growth or attenuation as downstream position increases.

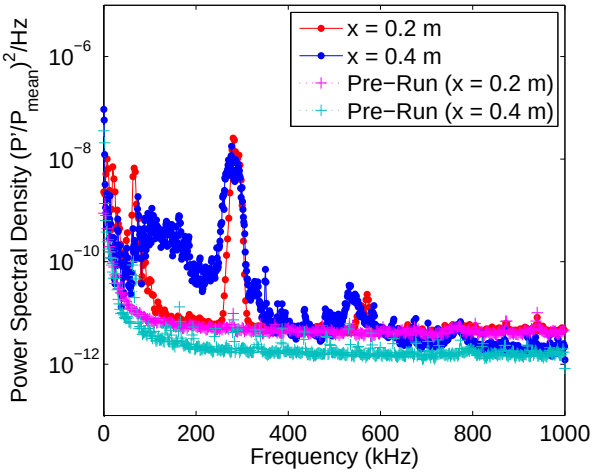

Figure 23: Spectra for one sensor at two different axial positions on two different runs. P_0 = 130.5 psia, quiet flow.

F. Summary of Experimental Results

Second-mode waves were successfully detected using PCB sensors on the compression cone. However, spatial resolution and calibration issues make it difficult to infer quantitative results. Under quiet flow, the second-mode waves grew with increasing Reynolds number to large amplitudes and become nonlinear, as evidenced by the appearance of harmonics. Frequency broadening and transition did not occur, however, even at computed N factors near 13 or higher. The width and peak frequency of the second-mode waves were predicted well by the calculations, but the waves did not appear to grow along the body. Transition was observed under noisy flow, but it was difficult to infer the exact transition location without additional instrumentation. The waves underwent a large change as they grew into turbulence, going from a single, well-defined peak to a broad peak with a high noise level, to turbulent flow. These preliminary results are promising and open a new venue for study of large second-mode waves and possibly transition under quiet flow. However, much work remains to be done.

IX. Instability in the Wake of an Isolated Roughness Element

A. Background

The effect of an isolated roughness on transition is being studied in an effort to develop a semi-empirical physics-based method for predicting transition. The BAM6QT features a unique laminar boundary layer under quiet flow. At lower Reynolds numbers, it is up to 3/4 in. thick on the nozzle wall. This boundary layer is thicker than that found on models and it is easier to make precise measurements using methods such as hot-wire anemometry. In addition, the thick boundary layer should reduce the instability frequencies and make them easier to detect. Measurements of the growth of instabilities should also be more feasible due to increased spatial resolution. These measurements will be useful in understanding the mechanisms that lead to transition. Temperature-sensitive paint images of the wake of the isolated roughness were reported in Reference 25. Quantitative measurements within the wake of the roughness are desired for comparison to computations. Initial measurements within the roughness wake have been made using a pitot probe and hot-wire probes. Under certain conditions, a 21 kHz oscillation can be seen. This oscillation is thought to be the first measured instability in the wake of a roughness at hypersonic speeds. Preliminary measurements will be reported here, with additional results to appear in References 26 and 27.

B. Roughness Element and Experimental Setup

A 5.97-mm-diameter (0.235-in.-diameter) Starrett model 263L–38TN micrometer head was used as a roughness element. The height of the cylindrical roughness element (k) can be changed from 0.00 mm to 24.31 mm and is accurate to ± 0.05 mm. The roughness height was adjusted prior to each test using the micrometer readout on the outside of the tunnel. The roughness element was located in the test section of the BAM6QT at tunnel coordinate $z = 1.924$ m (75.749 in.), mounted in a specially-designed circular insert in the upstream window blank. The four upstream windows of the BAM6QT test section are interchangeable, allowing the roughness element to be placed on either the lower wall or the side wall of the test section. The lower-wall configuration was used for hot-wire and pitot-probe measurements. Three locations in the circular insert allow the spanwise position of the roughness element to be changed, so that measurements can be taken off the center of the wake. The circular insert has a location in the center as well as ± 2 diameters off-center.

Either a Kulite (model XCQ-062-15A) pressure-transducer pitot probe or a hot-wire probe can be mounted on a 62°-angled probe support to make measurements in the tunnel centerplane. Figure 24a shows the typical setup for the wake measurements, looking upstream in the nozzle. The probe is held by the probe support, which is suspended from the top of the nozzle. The roughness element is installed on the bottom wall of the tunnel. The probe can be traversed in the wall-normal direction during a run. In addition, the streamwise position of the probe can be changed between runs. Figure 24b shows a close view of the probe in the wake of the roughness element. In the photo, the roughness is installed in the off-center position. Using this setup, the mean pitot pressure and the pressure fluctuations were recorded for various freestream Reynolds numbers, roughness heights, and locations within the wake. The Kulite sensor is mounted in a 1/8-in.-diameter tube that has been rounded at the leading edge to reduce flow interference. For other tests, calibrated and uncalibrated hot-wire probes were used in lieu of the Kulite. The pitot probe and hot-wire probes were designed to be similar in size and shape. Each probe has advantages and disadvantages. The

pitot probe is robust and less susceptible to electronic noise from the traverse, however it interferes more with the flow due to its size and is at times subject to sensor resonance. The hot-wire probes break frequently, but offer high frequency response.

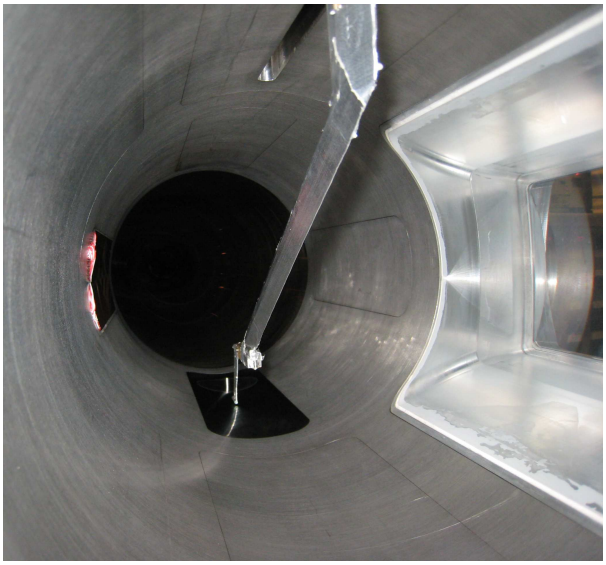

(a) Typical setup looking upstream.

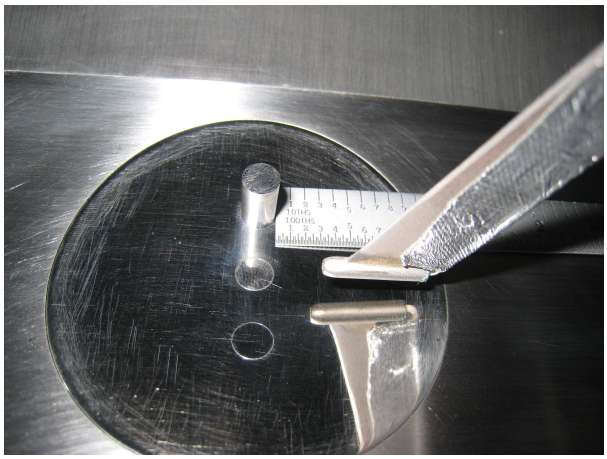

(b) Close view. Flow is from left to right. Scale showing tenths and hundredths of inches.

Figure 24: Typical setup for wake measurements using Kulite pitot probe. Setup for hot wires is similar.

C. Laminar Instability Near 21 kHz

An instability was seen for certain conditions in the wake of the roughness, when measuring off the centerline. Initial measurements were taken on the roughness centerline. Recent flow visualization by Danehy et al. showed large disturbances off the roughness centerline.[28] After reviewing the flow visualization results, it was decided to begin measuring off the centerline. A 21 kHz oscillation has been seen consistently when measuring two diameters off of the roughness centerline when the roughness height $k = 10.2$ mm. The oscillation is seen at initial stagnation pressures of $P_{0,i} = 80$ and 90 psia. The oscillation (Figure 25a) is large enough to be seen on the time trace, and has been seen using both the pitot probe and hot-wire probe at similar conditions. Figure 25b shows a typical pitot-probe spectrum with a clear peak at 21 kHz. The data were sampled at 2.0 MHz and were from a 0.05-s trace using 30 windows with 50% overlap. In the spectra the pressure fluctuation amplitude has been normalized by the theoretical freestream pitot pressure at Mach 6 (2.965% of the stagnation pressure). The fluctuation level of the peak was 4%. In the roughness wake, the power of the 21 kHz oscillation has been observed to peak at heights near the roughness height (10.2 mm) and to disappear in the freestream. For similar conditions with the roughness removed, the instability is not present.

Calibrated hot-wire measurements have shown that the oscillation grows downstream of the roughness, suggesting that the oscillation is a flow instability. The 0.0002-in. hot-wire was calibrated in the freestream of the BAM6QT and had a frequency response of 85 kHz. Several runs with the calibrated hot wire were performed at an initial stagnation pressure of 80 psia. Between runs, the hot wire was moved to different streamwise locations at a constant height above the wall in order to attempt to observe growth of the instability. This height was chosen to be 10.2 mm, the height at which the power of the oscillation was observed to be greatest. Spectra were calculated from a similar time during the run (at $t = 1.00 - 1.05$ s) such that flow conditions would be similar. The data were sampled at 2.0 MHz. The MATLAB mean-square spectrum function was used to compute the spectra and the power of the mass flux fluctuations was normalized by the mean mass flux.

Figure 26 shows the growth of the 21 kHz instability downstream of the roughness. The typical pre-run background noise spectrum is shown for comparison. Each spectrum downstream of the roughness shows a clear peak at 21 kHz. At 1.6 roughness diameters downstream, the power of the 21 kHz peak was roughly 1%

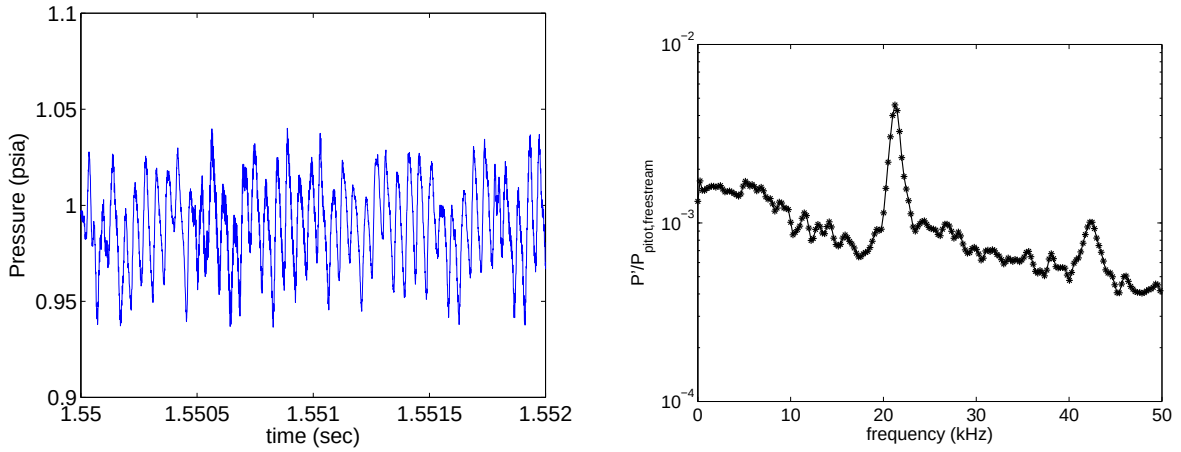

(a) Time trace.

(b) Root-mean-square spectra.

Figure 25: Kulite pitot probe time trace and spectra of 21kHz disturbance. Measuring two diameters off-center from roughness and 1.2 diameters downstream at a height of 8.5 mm. $P_{0,i} = 90$ psia and $k = 10.2$ mm.

of the mean mass flux and the baseline noise was roughly 0.1–1% . At 13 diameters downstream the power of the 21 kHz peak grew to 3% and the baseline noise levels grew higher. A peak at 65 kHz was observed at both 1.6 and 13 diameters downstream and could be a second instability. At 26.8 diameters downstream, the 21 kHz peak had a power of roughly 20% of the mean with higher baseline noise levels. When the probe was placed 7.6 diameters upstream of the roughness element, the spectrum was similar to the pre-run values, as expected for a laminar boundary layer. There was no evidence of the 21 kHz disturbance upstream of the roughness element, suggesting that the disturbance is not vibration of the probe support. Bench testing of the probe support has shown no high-frequency vibrations. The instability may result from a complex shock/boundary-layer interaction, however this seems unlikely.

Mean-flow and instability computations are being carried out for comparison to these experiments.[29] If good agreement can be obtained, that will validate both computation and experiment. The longer-term goal is to develop e^N-class methods for predicting transition in flight and in large wind tunnels, where measurements of the roughness wake and its instabilities do not appear feasible.

X. Conclusion

The Boeing/AFOSR Mach-6 Quiet Tunnel achieved a record quiet stagnation pressure of 163 psia in December 2008 and remains quiet at pressures greater than 160 psia. The tunnel shutdown process was observed to occur nearly simultaneously on multiple sensors under quiet flow conditions. Under noisy flow, the shutdown appeared to propagate slowly upstream through the nozzle. Testing of a 3° half-angle cone with a 15-mm blunt nosetip revealed that the tunnel started under certain conditions. Testing of various inserts in the new diffuser section continues. A new pipe insert extension was designed in order to start larger blunt models and increase run time. The insert was installed and preliminary tests indicated a 50% increase in run time.

A compression cone was designed with a constant-thickness boundary layer in order to produce continuous amplification of a narrow range of instability frequencies. This continuous amplification leads to large N factors. A geometry of this type could be used to cause natural transition under fully quiet flow. A study of five geometries was performed using the STABL software suite and an optimal design was selected and built. Computations at $P_0 = 140$ psia showed the growth of instabilities beginning at $x = 0.1$ m. Over the body of the cone, a single instability frequency near 280–290 kHz was predicted to cause maximum N factors near 16 at the end of the cone. The final compression cone design had a radius of curvature of 3 m with an initial nose half-angle of 2.0°. The nosetip had a 1 mm radius.

Under quiet flow, second-mode waves were measured on the compression cone near the frequencies and bandwidths predicted by the computations. Wave growth was not observed, possibly due to the poor spatial

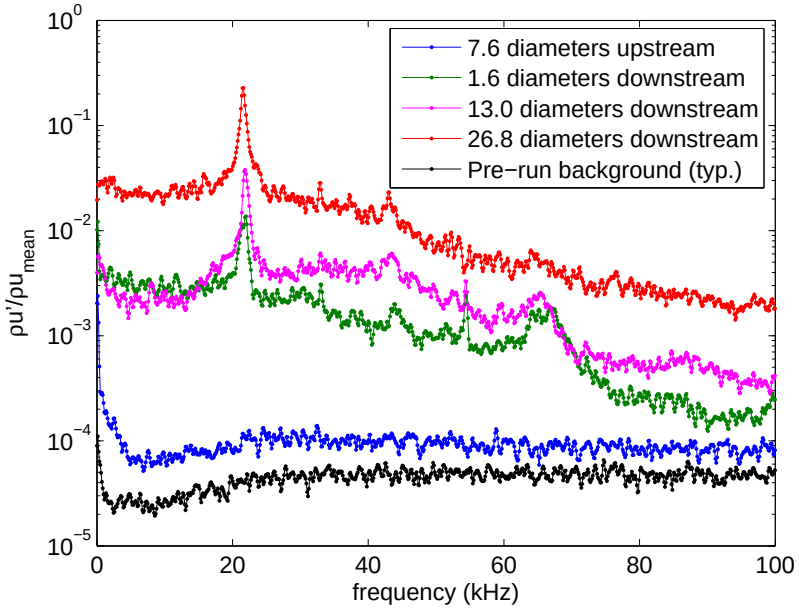

Figure 26: Root-mean-square spectra at a height of 10.2 mm above the wall, measuring two diameters off-center from the $k = 10.2$ mm roughness. All runs were at an initial stagnation pressure of 80 psia and the spectra are from $t = 1$ s during the run.

resolution of the PCB pressure sensors. Transition was not observed under quiet flow at $N \approx 13$ and above. Transition to turbulence was seen only under noisy conditions, though under noisy conditions the waves were less visible. Even though the pressure fluctuation amplitudes were uncertain, the results showed that a compression geometry can be used to study second-mode waves, non-linear effects, and possibly transition under quiet flow.

In an effort to help develop computational models for predicting roughness-induced transition, measurements of instabilities are sought in the wake of an isolated roughness element on the nozzle wall. The thick laminar boundary layer on the nozzle wall is ideal for making detailed wake measurements. An instability has been discovered in the roughness wake. The instability has been measured using two types of instrumentation and appears to grow downstream from the roughness.

Acknowledgments

This research was funded by AFOSR under grants FA9550-09-1-0191 and FA9550-08-1-0290, by NASA under grant 102361, by the NASA CUIP program, and by Sandia National Laboratory under contract 858548. Ponnampalam Balakumar of NASA Langley provided additional stability computations for the compression cone. Christopher Alba of AFRL/RBAC assisted in the analysis of the STABL results.

References

[1]C. R. Alba, H. B. Johnson, M. D. Bartkowicz, and G. V. Candler. Boundary Layer Stability Calculations of the HIFiRE Flight 1 Vehicle in the LaRC 20-Inch Mach 6 Air Tunnel. AIAA Paper 2008-505, January 2008.

[2]Steven P. Schneider. Hypersonic Laminar-Turbulent Transition on Circular Cones and Scramjet Forebodies. *Progress in Aerospace Sciences*, 40(1-2):1–50, February 2004.

[3]I. E. Beckwith and C. G Miller III. Aerothermodynamics and Transition in High-Speed Wind Tunnels at NASA Langley. *Annual Review of Fluid Mechanics*, 22:419–439, 1990.

[4]Steven P. Schneider. Effects of High-Speed Tunnel Noise on Laminar-Turbulent Transition. *Journal of Spacecraft and Rockets*, 38(3):323–333, May-June 2001.

[5]Steven P. Schneider. Flight Data for Boundary-Layer Transition at Hypersonic and Supersonic Speeds. *Journal of Spacecraft and Rockets*, 36(1):8–20, January-February 1999.

[6]F.-J. Chen, M. R. Malik, and I. E. Beckwith. Boundary-Layer Transition on a Cone and Flat Plate at Mach 3.5. *AIAA Journal*, 27(6):687–693, June 1989.

[7]Thomas J. Juliano, Steven P. Schneider, Selin Aradag, and Doyle Knight. Quiet-Flow Ludwieg Tube for Hypersonic Transition Research. *AIAA Journal*, 46(7):1757–1763, July 2008.

[8]Thomas J. Juliano. Nozzle Modifications for High-Reynolds-Number Quiet Flow in the Boeing/AFOSR Mach-6 Quiet Tunnel. Master's thesis, Purdue University School of Aeronautics & Astronautics, West Lafayette, IN, December 2006.

[9]Thomas J. Juliano, Erick O. Swanson, and Steven P. Schneider. Transition Research and Improved Performance in the Boeing/AFOSR Mach-6 Quiet Tunnel. AIAA Paper 2007-0535, January 2007.

[10]Matthew P. Borg, Steven P. Schneider, and Thomas J. Juliano. Inlet Measurements and Quiet Flow Improvements in the Boeing/AFOSR Mach-6 Quiet Tunnel. AIAA Paper 2006-1317, January 2006.

[11]Thomas J. Juliano, Rodrigo Segura, Matthew P. Borg, Katya Casper, Michael J. Hannon, Jr., Brad M. Wheaton, and Steven P. Schneider. Starting Issues and Forward-Facing Cavity Resonance in a Hypersonic Quiet Tunnel. AIAA Paper 2008-3735, June 2008.

[12]Craig R. Skoch, Steven P. Schneider, and Matthew P. Borg. Disturbances from Shock/Boundary Layer Interactions Affecting Upstream Hypersonic Flow. AIAA Paper 2005-4897, June 2005.

[13]L. Muller and A. Henckels. Visualization of High-Speed Boundary-Layer Transition with FPA Infrared Technique. *Notes on Numerical Fluid Mechanics*, 60:245–252, 1997.

[14]Heath B. Johnson, Christopher R. Alba, Matthew D. Bartkowicz, Travis W. Drayna, and Graham V. Candler. Design Optimization of Hypersonic Vehicles for Boundary-Layer Stability. AIAA Paper 2008-6221, August 2008.

[15]Heath B. Johnson and Graham V. Candler. Analysis of Laminar-Turbulent Transition in Hypersonic Flight Using PSE-Chem. AIAA Paper 2006-3057, June 2006.

[16]Heath B. Johnson, Chris R. Alba, Graham V. Candler, Matthew MacLean, Timothy Wadhams, and Michael Holden. Boundary-Layer Stability Analysis of the Hypersonic International Flight Research Transition Experiments. *Journal of Spacecraft and Rockets*, 45(2):228–236, March-April 2008.

[17]Ponnampalam Balakumar and Michael A. Kegerise. Receptivity of Hypersonic Boundary Layers over Straight and Flared Cones. Submitted for publication. 48th AIAA Aerospace Science Meeting, January 2010.

[18]Leslie M. Mack. Linear Stability Theory and the Problem of Supersonic Boundary-Layer Transition. *AIAA Journal*, 13(3):278–289, March 1975.

[19]E. F. Spina and C. B. McGinley. Constant Temperature Anemometry in Hypersonic Flow: Critical Issues and Sample Results. *Experiments in Fluids*, 17(6):365–374, 1994.

[20]Keisuke Fujii. Experiment of the Two-Dimensional Roughness Effect on Hypersonic Boundary-Layer Transition. *Journal of Spacecraft and Rockets*, 43(4):731–738, July-August 2006.

[21]Malte Estorf, Rolf Radespiel, Steven P. Schneider, and Heath B. Johnson. Surface-Pressure Measurements of Second-Mode Instability in Quiet Hypersonic Flow. AIAA Paper 2008-1153, January 2008.

[22]Katya M. Casper, Steven J. Beresh, John F. Henfling, Russell W. Spillers, Brian Puett, and Steven P. Schneider. Hypersonic Wind-Tunnel Measurements of Boundary-Layer Pressure Fluctuations. AIAA Paper 2009-4054, June 2009.

[23]Katya M. Casper. Hypersonic Wind Tunnel Measurements of Boundary Layer Pressure Fluctuations. Master's thesis, Purdue University School of Aeronautics & Astronautics, to appear August 2009.

[24]PCB. *Model 132A31 ICP® Dynamic Pressure Sensor Installation and Operating Manual*. `http://www.pcb.com/contentstore/docs/PCB_Corporate/Pressure/products/Manuals/132A31.pdf`.

[25]Katya M. Casper, Brad M. Wheaton, Heath B. Johnson, and Steven P. Schneider. Effect of Freestream Noise on Roughness-Induced Transition at Mach 6. AIAA Paper 2008-4291, June 2008.

[26]Brad M. Wheaton. Measurements in the Wake of an Isolated Roughness on the Nozzle Wall of the Mach-6 Quiet Tunnel. Master's thesis, Purdue University School of Aeronautics & Astronautics, to appear December 2009.

[27]Brad M. Wheaton and Steven P. Schneider. Measurements in the Wake of an Isolated Roughness Element at Mach 6. Submitted for publication. 48th AIAA Aerospace Science Meeting, January 2010.

[28]Paul M. Danehy, Brett Bathel, Christopher Ivey, Jennifer A. Inman, and Stephen B. Jones. NO PLIF Study of Hypersonic Transition over a Discrete Hemispherical Roughness Element. AIAA Paper 2009-394, January 2009.

[29]Patrick T. Greene, Jeff D. Eldredge, Xiaolin Zhong, and John Kim. A Numerical Study of Purdue's Mach 6 Tunnel with a Roughness Element. AIAA Paper 2009-174, January 2009.